

Novel Nano-composites SDC–LiNaSO₄ as Functional Layer for ITSOFC

Weiming Lv · Ze Tong · Yi-Mei Yin · Jiewei Yin · Zi-Feng Ma

Received: 8 December 2014 / Accepted: 28 February 2015 / Published online: 4 April 2015
© The Author(s) 2015. This article is published with open access at Springerlink.com

Abstract As an ionic conductive functional layer of intermediate temperature solid oxide fuel cells (ITSOFC), samarium-doped ceria (SDC)–LiNaSO₄ nano-composites were synthesized by a sol–gel method and their properties were investigated. It was found that the content of LiNaSO₄ strongly affected the crystal phase, defect concentration, and conductivity of the composites. When the content of LiNaSO₄ was 20 wt%, the highest conductivity of the composite was found to be, respectively, 0.22, 0.26, and 0.35 S cm⁻¹ at temperatures of 550, 600, and 700 °C, which are much higher than those of SDC. The peak power density of the single cell using this composite as an interlayer was improved to, respectively, 0.23, 0.39, and 0.88 W cm⁻² at 500, 600, and 700 °C comparing with that of the SDC-based cell. Further, the SDC–LiNaSO₄(20 wt%)-based cell also displayed better thermal stability according to the performance measurements at 560 °C for 50 h. These results reveal that SDC–LiNaSO₄ composite may be a potential good candidate as interlayer for ITSOFC due to its high ionic conductivity and thermal stability.

Keywords Nano-composite · SDC–LiNaSO₄ · Ionic conductor · Solid oxide fuel cell

1 Introduction

Solid-state ionic conductors and their applications as electrolytes and functional interlayers in intermediate temperature solid-state fuel cells (ITSOFC) have attracted much attention in the past few years [1–5]. This is because ionic conduction in either electrolyte or electrode is crucial to good performance of a fuel cell [6–8], and it is strongly desired to look for new ionic (oxide ion and proton) conductors operating at low and intermediate temperatures [9,

10]. The use of ceria-based materials, especially samaria- or gadolinia-doped ceria (SDC or GDC) as electrolyte or as functional layers between electrolyte and electrode, can significantly lower the operation temperature and increase the performance of solid oxide fuel cells due to their higher oxide ion conductivity (0.02 S cm⁻¹ at 700 °C) [11, 12]. The reason is that the ceria-based interlayer can reduce ohmic resistance and electrode polarization by increasing the electrical and ionic conduction at interface, blocking the inter-diffusion of elements and decreasing the thermal mismatch between electrode and electrolyte [3, 13]. Therefore, the enhanced ionic conductivity of the interlayer is important to improve the performance of a cell. It has been turned out that a very efficient method of enhancing the conductivity of ionic conductors is to decorate the grain boundaries with surface active second-phase particles [14]. Zhu et al. [15], Gao et al. [16], and Xia et al. [17] reported that composite electrolytes made of SDC and carbonates can promote the conductivity of SDC for one order of magnitude at 400–500 °C. They also proposed the mechanism for carbonates improving the ion conductivity

W. Lv · Y.-M. Yin (✉) · J. Yin · Z.-F. Ma
Shanghai Electrochemical Energy Devices Research Center,
School of Chemistry and Chemical Engineering, Shanghai Jiao
Tong University, Shanghai 200240, People's Republic of China
e-mail: yimei@sjtu.edu.cn

Z. Tong
Shanghai Research and Development Center for Polymer
Materials, Shanghai 200235, People's Republic of China

of the composite electrolytes. When the temperature reaches the melting point of the second phase salt, the molten salt fills in the voids between SDC particles and thus greatly increases the concentration of defects. This will increase the interfacial area between salts and SDC and also significantly accelerates the ion conduction velocity in the grain boundary. However, the molten phase of the carbonate salts is vulnerable under long-time heating by losing mass as operating at low and intermediate temperatures (400–700 °C), and then results in instability of a cell.

In this paper, we choose alkali double sulfate LiNaSO_4 as the second phase to prepare SDC– LiNaSO_4 (0–30 wt%) composites because LiNaSO_4 shows superionic conducting property at 514–615 °C [18]. We suppose that SDC– LiNaSO_4 composites may display enhanced conductivity and higher stability than SDC–carbonate composites in intermediate temperature. The physical–chemical properties including conductivity of SDC–sulfate composites were characterized. Power densities of the cells using pure SDC and SDC– LiNaSO_4 (20 wt%) as interlayers between yttria-stabilized zirconia (YSZ) electrolyte and $\text{Pr}_{0.5}\text{Sr}_{0.5}\text{Fe}_{0.8}\text{Cu}_{0.2}\text{O}_{3-\delta}$ (PSFC) [19] cathode were also compared.

2 Experimental

2.1 Preparation of SDC ($\text{Ce}_{0.8}\text{Sm}_{0.2}\text{O}_{1.90}$) and SDC– LiNaSO_4

A sol–gel method was used to synthesize SDC. The typical process is that cerium nitrate and samarium nitrate were dissolved into deionized water with a molar ratio of $n_{\text{Ce}^{3+}}:n_{\text{Sm}^{3+}} = 4:1$. Then EDTA and citric acid were added in the solution with the total molar ratio of $n_M:n_{\text{EDTA}}:n_{\text{CA}} = 1:1:1.2$. The pH of the solution was adjusted to pH 7–8 by adding ammonia. After that, the solution was heated and stirred at about 85 °C until it turned into a transparent gel. The gel was dried at 250 °C for 5 h and then a solid precursor was obtained. The precursor was finally calcined at 500 °C for 5 h to produce the SDC powder.

LiNaSO_4 was prepared by mixing $\text{Li}_2\text{SO}_4\cdot\text{H}_2\text{O}$ and Na_2SO_4 with a molar ratio of 1:1, ball-milling for 2 h, and calcining at 600 °C for half an hour. The as-prepared SDC and LiNaSO_4 powders were mixed with proper mass ratio (0–30 wt% for LiNaSO_4 powder) and pre-calcined at 750 °C for 1 h to obtain SDC– LiNaSO_4 composites. For X-ray diffraction (XRD) measurements, the LiNaSO_4 , SDC, and SDC– LiNaSO_4 composite powders were pressed to wafers under 100 MPa and sintered at 950 °C for 0.5 h. The composites and pure SDC were sintered, respectively, at 1050 and 1300 °C for 5 h for conductivity measurements.

2.2 Characterization

The compatibility of SDC and LiNaSO_4 , crystal structure, size, and morphology of composites were investigated by XRD (Rigaku D/max-2200/PC) and transmission electron microscope (TEM, JEM-2010/INCA). The Fourier transform infrared spectra (FTIR) measurements were performed on Paragon 1000 (Perkin Elmer USA). The phase transition and thermal stability were investigated by a thermal gravimetric (TG) differential scanning calorimetric (DSC) techniques.

The ionic conductivity measurements were performed via AC impedance method using an electrochemical workstation (Zahner IM6eX) under open-circuit voltage (OCV) in air. A 2-probe setup with silver paint electrodes was used. The applied frequency was ranged from 0.01 Hz to 1×10^6 Hz, and the signal amplitude was 50 mV. Measurements were conducted in 400–700 °C in a 25 °C interval.

Anode supported single cells were fabricated using YSZ as electrolyte with the thickness of about 18 μm . Two configurations of the cells respectively are Ni-YSZ/YSZ/SDC– LiNaSO_4 /PSFC (cell (a)) and Ni-YSZ/YSZ/SDC/PSFC (cell (b)). The interlayer was firstly screen printed onto YSZ side of Ni-YSZ/YSZ half-cell, and sintered, respectively, at 1050 and 1200 °C for 2 h for SDC– LiNaSO_4 (20 wt%) and SDC. Then, the PSFC cathode was screen printed onto the interlayer and sintered at 950 °C for 2 h. The current–voltage curves of single cells were measured by a sourcemeter (Keithley 2420, America). The anode side of the single cell was fed by humidified hydrogen with 3 vol% H_2O at the flow rate of 60 mL min^{-1} , while the cathode was exposed to air.

3 Results and Discussion

3.1 TG–DSC Analysis of LiNaSO_4

The TG and DSC curves of LiNaSO_4 are shown in Fig. 1. As a comparison, the results of binary carbonate Li_2CO_3 – Na_2CO_3 are also displayed. Two sharp endothermic peaks for DSC spectrum of LiNaSO_4 in position at about 521 and 615 °C are, respectively, attributed to a phase transition from hexagonal to body-centered cubic (bcc) phase and the melting of LiNaSO_4 [20]. The cations (Li^+ and Na^+) in the bcc phase have a high mobility according to a “paddle-wheel mechanism”, in which the strongly coupled rotational motion of the translational static sulfate ions enhances the mobility of the cations. This is the reason that LiNaSO_4 was reported be a superionic conductor at high temperature [18, 21, 22]. The TG curve of LiNaSO_4 in Fig. 1 displays that the weight is almost unchanged in

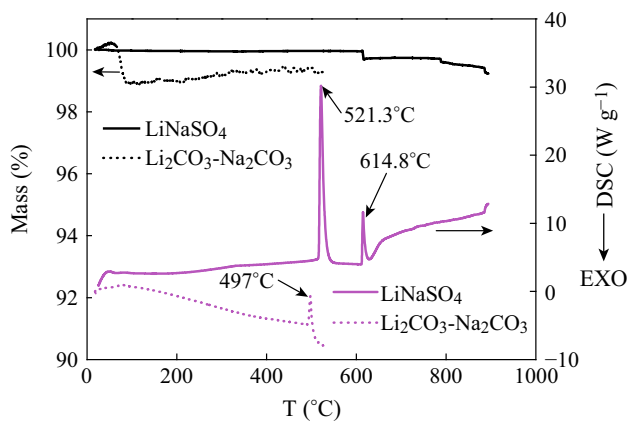


Fig. 1 TG and DSC curves of LiNaSO_4 and $\text{Li}_2\text{CO}_3\text{-Na}_2\text{CO}_3$

60–615 °C, and only a small weight loss of 0.24 % occurred above the melting point of 615 °C. With further increase in the temperature, no weight loss occurred in 615–788 °C in the melting process of LiNaSO_4 , indicating that the material is thermally stable up to about 788 °C. Comparing with the binary salt $\text{Li}_2\text{CO}_3\text{-Na}_2\text{CO}_3$ (dotted lines) whose melting point is 497 °C, LiNaSO_4 shows relative higher thermal stability in the intermediate temperature range of 500–700 °C.

3.2 Compatibility, Phase Structure, Size, and Morphology of SDC– LiNaSO_4

The XRD patterns of pure LiNaSO_4 , SDC, and SDC– LiNaSO_4 (10–30 wt%) wafers are shown in Fig. 2a. The crystallite size and the volume of crystal unit cell were calculated using Scherrer's formula and are listed in Table 1. It can be seen that no alien peaks appear except of LiNaSO_4 and SDC, indicating that no reaction occurred between LiNaSO_4 and SDC in the calcined and test processes. However, the intensity of SDC peaks was enhanced with the addition of LiNaSO_4 , especially for the 30 wt% sample. Contrarily, the intensity of LiNaSO_4 peaks was significantly reduced and only the peak at about $2\theta = 23^\circ$ was identified. These results demonstrate that the crystallization of SDC was slightly promoted by LiNaSO_4 , whereas the crystallization of LiNaSO_4 was suppressed evidently by the presence of SDC. The crystallite sizes of all samples are in nanoscale as shown in Table 1. The peak positions for both SDC and LiNaSO_4 were found to shift to lower 2θ with increasing x as shown in Fig. 2a. This reveals the enlargement of interplanar crystal spacing and lattice expansion occurred for both constituents of the composites compared to pure SDC and LiNaSO_4 . The lattice expansion was also confirmed by the calculated volume of crystal unit cell of SDC (Table 1). This may be attributed to the formation of more defects/vacancies during the quenching process. Because of the radius difference between cations (Li^+ , Na^+) and anion (SO_4^{2-}), LiNaSO_4 is more likely to form

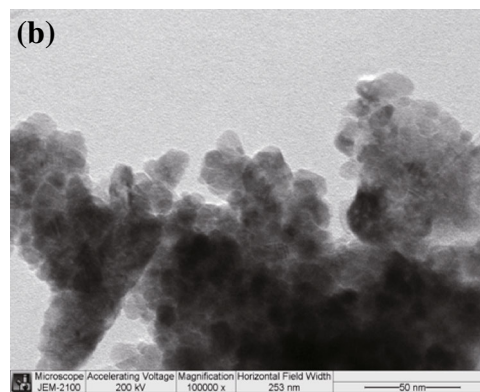
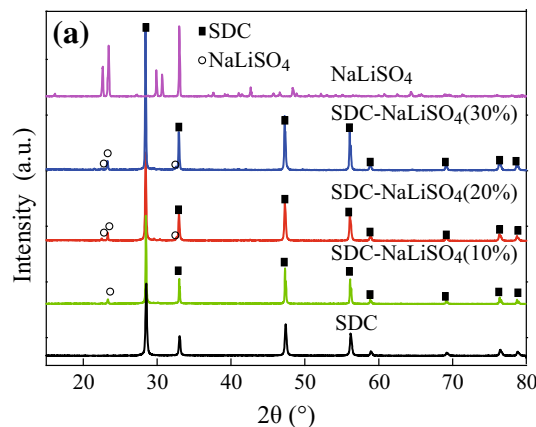


Fig. 2 a XRD patterns of pure LiNaSO_4 , SDC, and SDC– LiNaSO_4 (10–30 wt%) wafers sintered at 950 °C for 0.5 h; b TEM image of SDC– LiNaSO_4 (20 wt%) powders calcined at 750 °C for 1 h

Frenkel defects, i.e., $\text{M}_i\cdot$ and V_M' ($M = \text{Li}, \text{Na}$), which are mainly exist in the interstitial of a crystal material. The production of interstitial defects will lead to lattice expansion. The formation of defects in the lattice of LiNaSO_4 would cause lattice distortion, which would be expected to be reflected in the infrared spectra of the material.

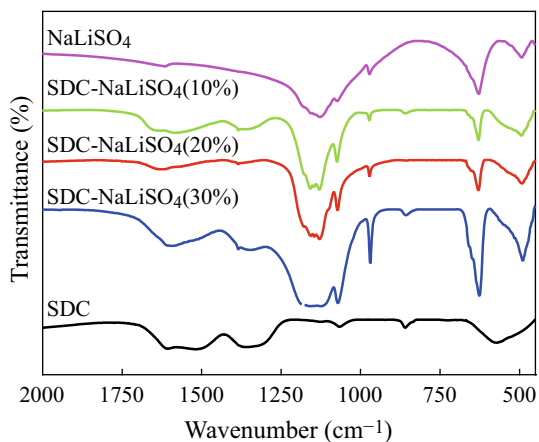
The representative TEM image of SDC– LiNaSO_4 (20 wt%) powder calcined at 750 °C for 1 h is shown in Fig. 2b. It clearly shows 10–20 nm round-shaped agglomerated nanocrystallites of SDC– LiNaSO_4 (20 wt%).

3.3 FTIR Analysis

Figure 3 shows the FTIR spectra of pure LiNaSO_4 , SDC, and SDC– LiNaSO_4 composites. In crystalline solids of LiNaSO_4 , the vibration, stretching, and bending of sulfate groups are influenced by the existence of defects and symmetry variations caused by structural environment change. The appearance of $\nu_1 = 971 \text{ cm}^{-1}$ and $\nu_2 = 492 \text{ cm}^{-1}$ in pure LiNaSO_4 indicates the decrease of symmetry of SO_4^{2-} ions due to the formation of the lattice defects [20]. As symmetry reduced further, the degeneracy in ν_2 , ν_3 , and ν_4 may be expected to be wholly or partially

Table 1 The crystallite size and unit cell volume of the samples in Fig. 2a

Samples	SDC	10 wt%	20 wt%	30 wt%	LiNaSO ₄
Crystallite size (nm)	47.2	58.5	60.9	79.9	69.2
Vol (Å ³)	159.1	159.2	160.4	160.4	495.7

**Fig. 3** FTIR spectra for LiNaSO₄, SDC, and SDC–LiNaSO₄ (10–30 wt%) composites at room temperature

removed. This is confirmed by the broadening adsorption peak of $\nu_3 = 1131 \text{ cm}^{-1}$ and the split ν_4 adsorption at 628 and 650 cm^{-1} for composites. The triply degenerate mode ν_3 is wholly split for composites with 10–20 wt% LiNaSO₄ as shown in Fig. 3. Moreover, for LiNaSO₄, a new absorption appears at $\nu = 1073 \text{ cm}^{-1}$. In existence of SDC, the relative intensity of this absorption increases and the peak position shifts to a higher wavenumber value along with the appearance of another new weak absorption at $\nu = 1180 \text{ cm}^{-1}$. These may result from interaction of the defects with the asymmetric stretching mode ν_3 . Therefore, IR spectra indirectly demonstrate the formation of defects (more likely Frenkel defects) in LiNaSO₄ and the concentration of the defects increases with 10–20 wt% content. It should be noted that for 30 wt% samples all the relative intensities of ν_1 – ν_4 absorption increase significantly. This indicates that the amplitude of motions, such as vibration, stretching, and bending of sulfate groups, is obviously enhanced due to the structural environment change induced possibly by strong interactions between SDC and LiNaSO₄. This may hinder the rotational motion of sulfate groups, and therefore decrease the mobility of the cations (Li⁺ and Na⁺).

3.4 Conductivity of SDC–LiNaSO₄

Conductivities of SDC and composites were determined applying the complex plane impedance analysis. Generally, three successive arcs can be observed in the complex impedance plane plots of polycrystalline solid ionic

conductors, which originated, respectively, from the bulk conduction (corresponding to arc1), grain boundary resistance (corresponding to arc2), and ion transfer resistance at the electrolyte–electrode surface (corresponding to arc3 or a tail) in sequence of decreasing frequency [23–25]. The total resistance of the solid conductor is the sum of bulk resistance and grain boundary resistance, and it can be conveniently converted to conductivity by considering the thickness (l) and area of the sample using the equation of $\sigma = l/RA$.

However, at a particular temperature, only parts of the three arcs appear because of the limited frequency range used in experiments. With increasing temperature, the arcs shifted to higher frequencies, leading to successive disappearance of arc1 or both arc1 and arc2. The typical complex impedance plots of pure SDC and SDC–LiNaSO₄ (20 wt%) composite at 600 °C are shown in Fig. 4a. The total resistances are indicated by arrows in the figure. The Arrhenius plots of conductivity for SDC and SDC–LiNaSO₄ (10–30 wt%) composites are shown in Fig. 4b. Comparably, the plot for the conductivity of SDC–(Li₂CO₃–Na₂CO₃) (20 wt%) composite is also illustrated. The conductivity of pure SDC increases linearly with temperature. From the slope, the apparent activation energy $E_a = 0.96 \text{ eV}$ was calculated, whereas the conductivities for all composites increase rapidly around the phase transition temperature of LiNaSO₄. It can be seen that the SDC–LiNaSO₄ (20 wt%) composite exhibits the highest conductivity at all testing temperatures compared with other SDC–LiNaSO₄ composites. For example, it reached 0.009 and 0.217 S cm^{-1} at 500 and 550 °C, respectively. The activation energy E_a decreases from 1.28 eV (below the transition temperature) to 0.30 eV (above the transition temperature) which are less than those of SDC–carbonate composites (1.47 and 0.33 eV below and above the transition temperature, respectively). Moreover, the conductivity of SDC–LiNaSO₄ (20 wt%) is much higher than that of SDC–(Li₂CO₃–Na₂CO₃) (20 wt%) at intermediate temperatures above 525 °C.

For single-phase SDC, the migration of ions is a thermally activated process. The ionic conductivity σ can be described by the Arrhenius equation of

$$\sigma T = \sigma_0 \exp(-E_a/kT),$$

where σ_0 is a pre-exponential factor, E_a is the activation energy, k is the Boltzmann constant, and T is the absolute

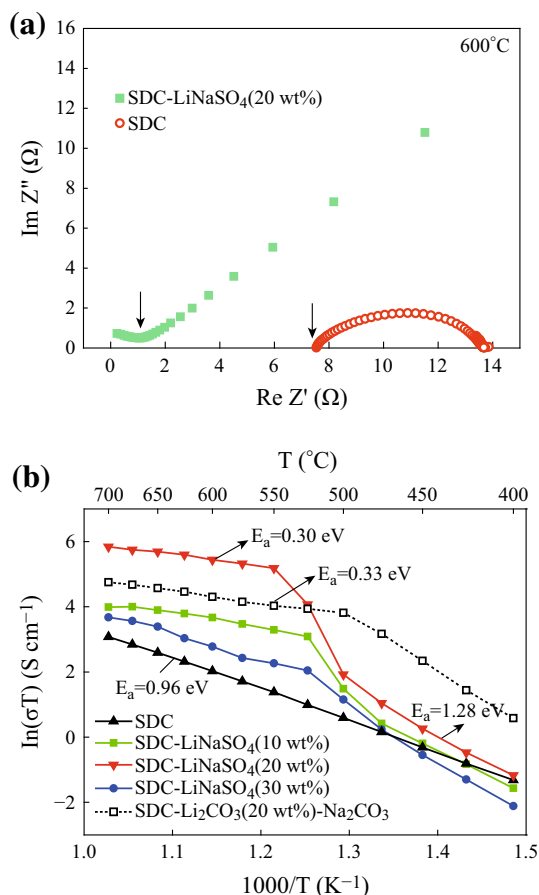


Fig. 4 **a** Complex impedance plane plots for pure SDC and SDC–LiNaSO₄ (20 wt%) composite at 600 °C; **b** Arrhenius plots for conductivity of SDC, SDC–LiNaSO₄ (10–30 wt%), and SDC–(Li₂CO₃–Na₂CO₃) (20 wt%) composites

temperature. σ_0 is related to two major parameters of the concentration of mobile ions (n) and the ion jump distance (d). From the equation, the decrease of σ_0 and E_a will result in increase of the material conductivity [26]. However, some limitations exist for the conductivity enhancement of doped single-phase oxides such as SDC and YSZ: (i) high E_a values of 1.0 eV (0.96 eV in the case of SDC as shown in Fig. 4b) result from the high activation energy for the formation of oxygen vacancy, the high migration energy for transport of the oxygen ion in the confined lattice, and the strong interaction between vacancies and cations; (ii) high σ_0 resulted from two aspects of low concentration of charge carriers due to limited doping concentration and the short jumping distance confined in a unit cell, i.e., of the order of some Angstrom.

An effective solution for above limitation is to introduce second phase to stabilize and modify the surface properties of single-phase oxides in nanoscale [27]. In nano-sized two-phase composite materials consisting of two ionic conductors, a high concentration of mobile ions, long jumping distance, and low activation energy can be

obtained at the interfaces/grain boundaries without the structural limitations of the bulk. The interfacial ionic conduction mechanism allows ions to move on particles' surface or interface through high conductivity pathways. It has been experimentally found that superionic conduction occurs for the SDC–carbonate two-phase materials, e.g., SDC–Na₂CO₃, SDC–CaCO₃, SDC–Li₂CO₃–Na₂CO₃, and SDC–Li₂CO₃–Na₂CO₃–K₂CO₃ [16, 28–30].

Different from SDC–carbonate composites in which the significantly enhanced conductivity in 400–500 °C results from the melting process of the carbonates at the elevated temperature, the enhanced ionic conductivity of SDC–LiNaSO₄ composites in 500–550 °C may be co-contributed by the high mobility of cations (Li⁺ and Na⁺) in bcc phase of LiNaSO₄ at higher temperatures and the increased mobility of ions (Li⁺, Na⁺, and oxide ions) in the bulk as well as at the interface of the two constituents in the composites. The possible reasons may be as follows: (i) The discontinuity of the conductivities for the composites at 500–550 °C agrees well with the phase transition of LiNaSO₄ (514–560 °C) instead of melting process as seen in Figs. 1 and 4; (ii) The lattice expansion and formation of more defects in the bulk of the two constituents of the composites, as analyzed in XRD and FTIR results, are beneficial to the migration of ions because ions diffuse faster in open lattice and in crystal with more defects; (iii) The bcc phase of LiNaSO₄ is plastic crystal (rotator phase) [18], which is softer than hexagonal phase and may enhance the mobility of ions at the interface of SDC and LiNaSO₄ at higher temperatures. The contribution of the migration of sulfate groups to the enhanced conductivity of the composites could be neglected because the diffusion coefficient of sulfate group is 4 orders of magnitude smaller compared to the monovalent cations (Li⁺ and Na⁺) [18]. In addition, proton conduction plays an important role for solid sulfate electrolytes when they are tested in hydrogen concentration cells or used as electrolyte in fuel cells [31–34]. However, in the case of this paper, for example, the conductivities were tested in air, and SDC–LiNaSO₄ (20 wt%) was used as interlayer between YSZ electrolyte (oxide ion conductor) and cathode, the contribution of proton conduction to the conductivity of the composites should be insignificant.

When LiNaSO₄ grains are not effectively contacted with each other just like that in SDC–LiNaSO₄ (10 wt%), or when the rotational motion of sulfate groups in LiNaSO₄ is hindered just like that in SDC–LiNaSO₄ (30 wt%), the conductivity of composites will reduce. Thus, the conductivity will reach the highest value when the mass ratio of LiNaSO₄:SDC is optimized just like that in SDC–LiNaSO₄ (20 wt%). Moreover, the solid nature of SDC–LiNaSO₄ composites enables them more thermally stable at intermediate temperatures of 500–600 °C.

3.5 Single-Cell Performance with SDC and SDC–LiNaSO₄ (20 wt%) Interlayers

The *I–V* and *I–P* curves of single cells with SDC–LiNaSO₄ (20 wt%) composite (cell (a)) or pure SDC (cell (b)) interlayer are shown in Fig. 5, respectively. It can be seen that the peak power density of cell (a) is significantly improved comparing with that of cell (b). For example, the peak power density of cell (a) is 0.88 W cm^{–2}, while it is only 0.68 W cm^{–2} for cell (b) at 700 °C. The improvement of the performance is mainly due to the contribution of the higher conductivity of SDC–LiNaSO₄ (20 wt%) interlayer. This indicates that SDC–LiNaSO₄ is a promising candidate to replace the conventional SDC/GDC as the interlayer between YSZ and cathode. Much higher performance may be achieved by optimizing cathode microstructure and decreasing the thickness of YSZ electrolyte further.

The cross-sectional SEM images of the single cells are shown in Fig. 6. One can see that three layers between the porous PSFC cathode, SDC or SDC–LiNaSO₄ (20 wt%), and the dense YSZ electrolyte contact each other well. The thickness of the interlayer is about 3 μm. No obvious

delamination or cracks were observed at interfaces, suggesting a good compatibility between these materials.

3.6 The Stability of Single Cells

The thermal stability of SDC–LiNaSO₄ (20 wt%) was examined by recording the performance of single cells at 560 °C for 50 h (shown in Fig. 7). The power density of both cells increases firstly and then decreases slowly. The initial improvement in performance of the cells may be attributed to re-arrangement in microstructure and activation of each constituent in the cells, whereas the subsequent decline may be due to the slight leak of gas and aggregation of cathode particles. The fluctuation of the performance of cell (a) is smaller than that of cell (b), indicating that the thermal stability of SDC–LiNaSO₄ (20 wt%) composite is better than that of pure SDC.

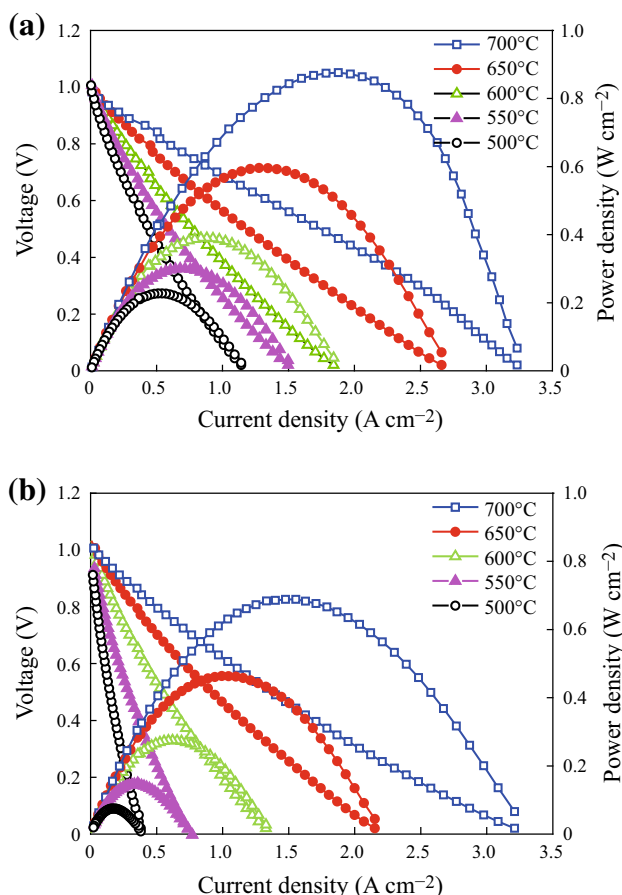


Fig. 5 *I–V* and *I–P* curves of single cells **a** using SDC–LiNaSO₄ (20 wt%) and **b** using SDC as interlayer

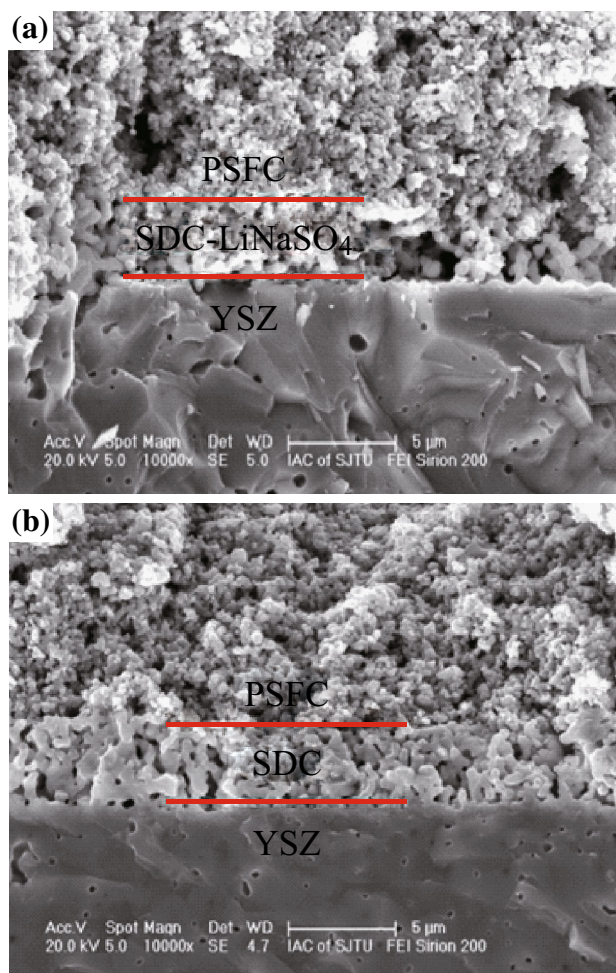


Fig. 6 The SEM images of the cross section of single cells **a** with SDC–LiNaSO₄ (20 wt%) interlayer; **b** with SDC interlayer

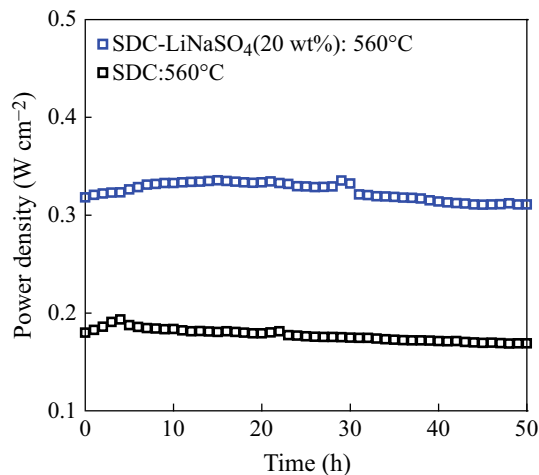


Fig. 7 The time relationship of the power density of single cells at 560 °C for 50 h with SDC–LiNaSO₄ (20 wt%) interlayer (*blue square*) and with SDC interlayer (*black square*). (Color figure online)

4 Conclusions

We prepared nano-composites SDC–LiNaSO₄ with high ionic conductivity and thermal stability. The composites' properties with different mass ratios were investigated and SDC–LiNaSO₄ (20 wt%) was found to have the highest conductivity at intermediate temperature of 500–700 °C. As a functional layer of IT-SOFC, the cell performance was improved significantly. Our results indicate that SDC–LiNaSO₄ may be a penitential ionic conductive functional material for IT-SOFC.

Acknowledgments This research was supported by the Natural Science Foundation of China (21173147 and 21376143) and 973 Program of China (2014CB239700). Thanks were also given to the support of Science and Technology Commission of Shanghai Municipality (14DZ22250800).

Open Access This article is distributed under the terms of the Creative Commons Attribution 4.0 International License (<http://creativecommons.org/licenses/by/4.0/>), which permits unrestricted use, distribution, and reproduction in any medium, provided you give appropriate credit to the original author(s) and the source, provide a link to the Creative Commons license, and indicate if changes were made.

References

1. N.Q. Minh, Ceramic fuel cells. *J. Am. Ceram. Soc.* **76**(3), 563–588 (1993). doi:[10.1111/j.1151-2916.1993.tb03645.x](https://doi.org/10.1111/j.1151-2916.1993.tb03645.x)
2. S. Singhal, Solid oxide fuel cells for power generation. *WIREs Energy Environ.* **3**(2), 179–194 (2014). doi:[10.1002/wene.96](https://doi.org/10.1002/wene.96)
3. J.H. Song, M.G. Jung, H.W. Park, H.T. Lim, The effect of fabrication conditions for GDC buffer layer on electrochemical performance of solid oxide fuel cells. *Nano-Micro Lett.* **5**(3), 151–158 (2013). doi:[10.1007/BF03353744](https://doi.org/10.1007/BF03353744)
4. L.D. Fan, C.Y. Wang, M.M. Chen, B. Zhu, Recent development of ceria-based (nano) composite materials for low temperature

- ceramic fuel cells and electrolyte-free fuel cells. *J. Power Sources* **234**, 154–174 (2013). doi:[10.1016/j.jpowsour.2013.01.138](https://doi.org/10.1016/j.jpowsour.2013.01.138)
5. D.S. Khaerudini, G.Q. Guan, P. Zhang, X.G. Hao, A. Abudula, Prospects of oxide ionic conductivity bismuth vanadate-based solid electrolytes. *Rev. Chem. Eng.* **30**(6), 539–551 (2014). doi:[10.1515/revce-2014-0020](https://doi.org/10.1515/revce-2014-0020)
6. J.W. Yin, Y.M. Yin, J. Lu, C.M. Zhang, N.Q. Minh, W.M. Zhang, Z.F. Ma, Nd_{0.5}Sr_{0.5}Fe_{0.8}Cu_{0.2}O_{3-δ}-xSm_(0.2)Ce_(0.8)O_(1.9) cobalt-free composite cathodes for intermediate temperature solid oxide fuel cells. *Int. J. Hydrogen Energy* **39**(31), 17852–17856 (2014). doi:[10.1016/j.ijhydene.2014.08.131](https://doi.org/10.1016/j.ijhydene.2014.08.131)
7. J.H. Song, M.Y. Park, H.W. Park, H.T. Lim, Single-step preparation of nano-homogeneous NiO/YSZ composite anode for solid oxide fuel cells. *Nano-Micro Lett.* **5**(2), 111–116 (2013). doi:[10.1007/BF03353737](https://doi.org/10.1007/BF03353737)
8. J.W. Yin, Y.M. Yin, J. Lu, C. Zhang, N.Q. Minh, Z.F. Ma, Structure and properties of novel cobalt-free oxides Nd_xSr_{1-x}-Fe_{0.8}Cu_{0.2}O_{3-δ} (0.3 ≤ x ≤ 0.7) as cathodes of intermediate temperature solid oxide fuel cells. *J. Phys. Chem. C* **118**(25), 13357–13368 (2014). doi:[10.1021/jp500371w](https://doi.org/10.1021/jp500371w)
9. H. Chen, K. Cheng, F. Ye, W.J. Weng, Preparation and characterization of graded SSC-SDC MIEC cathode for low-temperature solid oxide fuel cells. *Ceram. Int.* **37**(4), 1209–1214 (2011). doi:[10.1016/j.ceramint.2010.11.047](https://doi.org/10.1016/j.ceramint.2010.11.047)
10. C.R. Xia, M.L. Liu, Novel cathodes for low-temperature solid oxide fuel cells. *Adv. Mater.* **14**(7), 521–523 (2002). doi:[10.1002/1521-4095\(20020404\)14:7<521:AID-ADMA521>3.0.CO;2-C](https://doi.org/10.1002/1521-4095(20020404)14:7<521:AID-ADMA521>3.0.CO;2-C)
11. W.C. Wu, J.T. Huang, A. Chiba, Synthesis and properties of samaria-doped ceria electrolyte for IT-SOFCs by EDTA-citrate complexing method. *J. Power Sources* **195**(18), 5868–5874 (2010). doi:[10.1016/j.jpowsour.2009.12.098](https://doi.org/10.1016/j.jpowsour.2009.12.098)
12. M. Chen, B.H. Kim, Q. Xu, B.K. Ahn, W.J. Kang, D.P. Huang, Synthesis and electrical properties of Ce_{0.8}Sm_{0.2}O_{1.9} ceramics for IT-SOFC electrolytes by urea-combustion technique. *Ceram. Int.* **35**(4), 1335–1343 (2009). doi:[10.1016/j.ceramint.2008.06.014](https://doi.org/10.1016/j.ceramint.2008.06.014)
13. Z.G. Lu, X.D. Zhou, D. Fisher, J. Templeton, J. Stevenson, N.J. Wu, A. Ignatiev, Enhanced performance of an anode-supported YSZ thin electrolyte fuel cell with a laser-deposited Sm_{0.2}Ce_{0.8}O_{1.9} interlayer. *Electrochem. Commun.* **12**(2), 179–182 (2010). doi:[10.1016/j.elecom.2009.11.015](https://doi.org/10.1016/j.elecom.2009.11.015)
14. J. Maier, Nanoionics: ion transport and electrochemical storage in confined systems. *Nat. Mater.* **4**(11), 805–815 (2005). doi:[10.1038/nmat1513](https://doi.org/10.1038/nmat1513)
15. B. Zhu, S. Li, B.E. Mellander, Theoretical approach on ceria-based two-phase electrolytes for low temperature (300–600 °C) solid oxide fuel cells. *Electrochem. Commun.* **10**(2), 302–305 (2008). doi:[10.1016/j.elecom.2007.11.037](https://doi.org/10.1016/j.elecom.2007.11.037)
16. Z. Gao, J.B. Huang, Z.Q. Mao, C. Wang, Z.X. Liu, Preparation and characterization of nanocrystalline Ce_{0.8}Sm_{0.2}O_{1.9} for low temperature solid oxide fuel cells based on composite electrolyte. *Int. J. Hydrogen Energy* **35**(2), 731–737 (2010). doi:[10.1016/j.ijhydene.2009.10.090](https://doi.org/10.1016/j.ijhydene.2009.10.090)
17. C. Xia, Y. Li, Y. Tian, Q.H. Liu, Z.M. Wang, L.J. Jia, Y.C. Zhao, Y.D. Li, Intermediate temperature fuel cell with a doped ceria-carbonate composite electrolyte. *J. Power Sources* **195**(10), 3149–3154 (2010). doi:[10.1016/j.jpowsour.2009.11.104](https://doi.org/10.1016/j.jpowsour.2009.11.104)
18. R. Tarneberg, A. Lunden, Ion diffusion in the high-temperature phases Li₂SO₄, LiNaSO₄, LiAgSO₄ and Li₄Zn(SO₄)₃. *Solid State Ionics* **90**, 209–220 (1996). doi:[10.1016/S0167-2738\(96\)00399-2](https://doi.org/10.1016/S0167-2738(96)00399-2)
19. J. Lu, Y.M. Yin, Z.F. Ma, Preparation and characterization of new cobalt-free cathode Pr_{0.5}Sr_{0.5}Fe_{0.8}Cu_{0.2}O_{3-δ} for IT-SOFC. *Int. J. Hydrogen Energy* **38**(25), 10527–10533 (2013). doi:[10.1016/j.ijhydene.2013.05.164](https://doi.org/10.1016/j.ijhydene.2013.05.164)
20. S.W. Tai, B. Zhu, D.K. Peng, G.Y. Meng, Investigation on LiNaSO₄-Al₂O₃ ceramics as electrolytes for H₂/O₂ fuel cells.

- Mater. Res. Bull. **34**(10–11), 1651–1659 (1999). doi:[10.1016/S0025-5408\(99\)00161-0](https://doi.org/10.1016/S0025-5408(99)00161-0)
21. K.N. Ganesha, G. Govindaraj, Synthesis, characterization and ion conductivity study of nanocrystalline LiNaSO_4 . AIP Conf. Proc. **1512**, 386–387 (2013). doi:[10.1063/1.4791073](https://doi.org/10.1063/1.4791073)
 22. L. Larlsson, R.L. McGreevy, Mechanisms of ionic conduction in Li_2SO_4 and LiNaSO_4 Paddle wheel or percolation? Solid State Ionics **76**, 301–308 (1995). doi:[10.1016/0167-2738\(94\)00278-Z](https://doi.org/10.1016/0167-2738(94)00278-Z)
 23. J. Patakangas, Y. Ma, Y.F. Jing, P. Lund, Review and analysis of characterization methods and ionic conductivities for low-temperature solid oxide fuel cells (LT-SOFC). J. Power Sources **263**, 315–331 (2014). doi:[10.1016/j.jpowsour.2014.04.008](https://doi.org/10.1016/j.jpowsour.2014.04.008)
 24. Z.L. Zhan, T.L. Wen, H.Y. Tu, Z.Y. Lu, AC impedance investigation of samarium-doped ceria. J. Electrochem. Soc. **148**(5), A427–A432 (2001). doi:[10.1149/1.1359198](https://doi.org/10.1149/1.1359198)
 25. M. Benamira, A. Ringuede, L. Hildebrandt, C. Lagergren, R.N. Vannier, M. Cassir, Gadolinia-doped ceria mixed with alkali carbonates for SOFC applications: II—an electrochemical insight. Int. J. Hydrogen Energy **37**(24), 19371–19379 (2012). doi:[10.1016/j.ijhydene.2011.10.062](https://doi.org/10.1016/j.ijhydene.2011.10.062)
 26. J.B. Goodenough, Ceramic technology—oxide-ion conductors by design. Nature **404**(6780), 821–823 (2000). doi:[10.1038/35009177](https://doi.org/10.1038/35009177)
 27. Q.H. Liu, B. Zhu, Theoretical description of superionic conductivities in samaria doped ceria based nanocomposites. Appl. Phys. Lett. **97**(18), 183115 (2010). doi:[10.1063/1.3513375](https://doi.org/10.1063/1.3513375)
 28. B. Zhu, Functional ceria-salt-composite materials for advanced ITSOFC applications. J. Power Sources **114**(1), 1–9 (2003). doi:[10.1016/S0378-7753\(02\)00592-X](https://doi.org/10.1016/S0378-7753(02)00592-X)
 29. Y.D. Li, Z.B. Rui, C. Xia, M. Anderson, Y.S. Lin, Performance of ionic-conducting ceramic/carbonate composite material as solid oxide fuel cell electrolyte and CO_2 permeation membrane. Catal. Today **148**(3–4), 303–309 (2009). doi:[10.1016/j.cattod.2009.08.009](https://doi.org/10.1016/j.cattod.2009.08.009)
 30. Y.F. Ling, J. Patakangas, P.D. Lund, B. Zhu, An improved synthesis method of ceria-carbonate based composite electrolytes for low-temperature SOFC fuel cells. Int. J. Hydrogen Energy **38**(36), 16532–16538 (2013). doi:[10.1016/j.ijhydene.2013.05.136](https://doi.org/10.1016/j.ijhydene.2013.05.136)
 31. B. Zhu, B.E. Mellander, Proton conduction and diffusion in Li_2SO_4 . Solid State Ionics **97**(1–4), 535–540 (1997). doi:[10.1016/S0167-2738\(97\)00057-X](https://doi.org/10.1016/S0167-2738(97)00057-X)
 32. A. Lunden, B. Mellander, B. Zhu, Mobility of protons and oxygen ions in lithium sulfate and other oxyacid salts. Acta Chem. Scand. **45**(9), 981–982 (1991). doi:[10.3891/acta.chem.scand.45-0981](https://doi.org/10.3891/acta.chem.scand.45-0981)
 33. B. Heed, Proton conductivity in fuel cells with solid sulfate electrolytes. Solid State Ionics **46**(1–2), 121–125 (1991). doi:[10.1016/0167-2738\(91\)90139-3](https://doi.org/10.1016/0167-2738(91)90139-3)
 34. S.Y. Oh, T. Yoshida, G. Kawamura, H. Muto, A. Matsuda, Solid-state mechanochemical synthesis of CsHSO_4 and 1,2,4-triazole inorganic-organic composite electrolytes for dry fuel cells. Electrochim. Acta **56**(5), 2364–2371 (2011). doi:[10.1016/j.electacta.2010.11.035](https://doi.org/10.1016/j.electacta.2010.11.035)